Fault-tolerant Deadbeat Model Predictive Current Control for a Five-phase PMSM with Improved SVPWM*

Suleman Saeed[1], *Wenxiang Zhao*[1*], *Huanan Wang*[1], *Tao Tao*[1] *and Faisal Khan*[2]
(1. School of Electrical and Information Engineering, Jiangsu University, Zhenjiang 212013, China;
2. Department of Electrical and Computer Engineering, COMSATS University Islamabad, Abbottabad Campus, Abbottabad 22060, Pakistan)

Abstract: The main drawbacks of traditional finite set model predictive control are high computational load, large torque ripple, and variable switching frequency. A less complex deadbeat (DB) model predictive current control (MPCC) with improved space vector pulse-width modulation (SVPWM) under a single-phase open-circuit fault is proposed. The proposed method predicts the reference voltage vector in the α-β subspace by employing the deadbeat control principle on the machine predictive model; thus, the exhaustive exploration procedure is avoided to relieve the computational load. To perform the constant switching frequency operation and achieve better steady-state performance, a modified SVPWM strategy is developed with the same conventional structure, which modulates the reference voltage vector. This new approach is based on a redesigned and adjusted post-fault virtual voltage vector space distribution that eliminates the y-axis harmonic components in the x-y subspace and ensures the generation of symmetrical PWM pulses. Meanwhile, the combined merits of the DB, MPCC, and SVPWM methods are realized. To verify the effectiveness of the proposed control scheme, comparative experiments are performed on a five-phase permanent magnet synchronous motor (PMSM) drive system.

Keywords: Five-phase, fault-tolerant, permanent magnet, deadbeat model predictive control, space vector modulation

1 Introduction

Multi-phase machines have received substantial attention from the research community owing to their numerous advantages over their conventional three-phase counterparts, such as improved fault tolerance, better power distribution, and lower torque distortions [1-3]. These merits of multiphase machines are exploited in high-performance control applications [4-5]. The increased control degrees of freedom improve the fault tolerance of multiphase drives, even without additional hardware [2].

Manuscripts received April 21, 2021; revised June 21, 2021; accepted July 21, 2021. Date of publication September 30, 2021; date of current version July 28, 2021.
* Corresponding Author, E-mail: zwx@ujs.edu.cn
* Supported in part by the National Natural Science Foundation of China under Grant 52025073, in part by the Key Research and Development Program of Jiangsu Province under Grant BE2018107, and in part by the Priority Academic Program Development of Jiangsu Higher Education Institutions.
Digital Object Identifier: 10.23919/CJEE.2021.000030

Recently, traditional three-phase control schemes have been extended to multiphase configurations under normal and faulty operations. The most frequent fault in drives is the open-circuit fault, where the space distribution of the stator voltage vectors becomes irregular and complex. Typically, to realize fault-tolerant control, the magnetic motive force (MMF) should be kept undisturbed. Furthermore, with the loss of any phase, the torque ripple increases [6], and the remaining asymmetrical healthy phases cannot produce pre-fault rated torque, unless the stator rated current has no limit [7].

Most recently, model predictive control has been introduced in faulty multiphase drives owing to its superior advantages over conventional field-oriented control and direct torque control. However, this control method is more sensitive to parameter variations because precise machine model is crucial [8]. Generally, predictive control can be categorized based on the switching state generation technique. The conventional finite control set model predictive control (FCS-MPC) predicts the future control variables by utilizing the machine model and selects an optimal voltage vector from a finite control set, which lowers the error of a predefined cost function [9]. This selected voltage vector or switching state is directly applied without a modulation stage; however, the evaluation of all candidate vectors in one control period causes a high computational load. In addition, the application of a single voltage vector in one control period and the influence of the harmonic subspace components deteriorate the steady-state operation performance. The key solutions to the abovementioned problems in the conventional fault-tolerant FCS-MPC scheme for operation in five-phase and six-phase motors are presented in Refs. [10-14]. In Ref. [10], a simplified control set was proposed for a five-phase PM motor, which reduced the number of candidate vectors in a sampling period. However, the computational load was still high because of the predictions of the harmonic currents, and the duty optimization of a single vector was not sufficient for optimum performance. Moreover, in Ref. [11], pulse-width modulation (PWM) predictive control was studied for a six-phase PM motor under an open-circuit fault. A model predictive torque control was presented for a five-phase PMSM drive in Ref. [12], in which the reference voltage vector was synthesized from two selected vectors according to the space vector modulation principle. However, the tuning process of the weighting factors was difficult because of the inclusion of harmonic currents in the cost function. In Ref. [13], harmonic-less virtual voltage vectors were reported, and in Ref. [14], a model predictive current control method with continuous modulation was proposed, in which the post-fault voltage vector distribution was remodeled. This produced standard PWM waves, and the back electromotive force of the faulty phase was reimbursed. However, the multistep procedure caused complexity and a relatively high computational load.

The other type of conventional model predictive control is the modulated deadbeat model predictive control (DB-MPC), which uses a machine model and the deadbeat control principle to predict the reference voltage vector, after which a modulation stage generates the optimal PWM pulses [15]. This strategy preserves the fast dynamic response of FCS-MPC with further benefits, such as reduced online computational load, low torque ripple, and constant switching frequency. This scheme was introduced for the healthy operation of three-phase drives in Refs. [15-17]. In addition, in Refs. [18-19], it was studied for five-phase drives under health conditions in which the external modulation stage was not used. In Ref. [18], the computational burden was reduced considerably, and a single virtual voltage vector with duty optimization was applied in a control period. In contrast, in Ref. [19], a geometric principle was employed to select a second virtual voltage vector, which enhanced the steady-state performance. In leading studies, the DB-MPC method has not yet been extended to five-phase fault-tolerant operation.

Among modulation strategies, the traditional space vector pulse-width modulation (SVPWM) synthesizes a reference voltage vector from two adjacent voltage vectors and a zero vector [20]. In this technique, the DC bus voltage utilization increases along with a reduction in the torque ripple and stator current harmonics [21]. Moreover, the constant switching frequency operation can be performed. In Ref. [22], an SVPWM-based field-oriented control was proposed for a five-phase PM motor under an open-circuit fault of one phase. However, the same decoupling matrix was used before and after the fault, so the narrow bandwidth of the PI current controllers was unable to remove the error effectively. In addition, high distortions in the stator phase currents were present because the harmonic regulation was ignored. A five-phase SVPWM fault-tolerant control was studied in Ref. [23], in which a PI current control loop was added for harmonic regulation. Although the current, torque, and efficiency were enhanced, the complexity of the system was high because extra tuning effort was required for the third current controller. In Refs. [24-25], the different aspects of PI controller design and implementation are discussed. Therefore, the existing five-phase fault-tolerant SVPWM approaches are complex, with generally slow dynamic responses of the PI regulators [26] and unacceptable harmonic distortions.

In this paper, a deadbeat model predictive current control (DB-MPCC) with an improved symmetrical SVPWM is proposed for a five-phase PMSM under a single-phase open-circuit fault. This strategy solves the optimization problem by predicting the reference voltage vector. The main contribution of this study is the development of a modified fault-tolerant SVPWM scheme with the same conventional structure as the healthy SVPWM, in which a harmonic-less redesigned virtual voltage vector space distribution serves as available vectors to synthesize the reference voltage vector. This paper is organized as follows. Section 2 describes the post-fault predictive model of a five-phase drive under an open-circuit fault. In Section 3, the proposed strategy is presented. The experimental results are analyzed in Section 4. Finally, Section 5 summarizes the conclusions of this study.

2 Post-fault predictive model of five-phase drive

The five-phase PMSM is fed through a two-level five-phase voltage source inverter. The configuration of the drive system is illustrated in Fig. 1. After the occurrence of the single-phase open-circuit fault, the five-phase inverter is reduced to a four-phase inverter and loses half of the available switching states, from 32 (2^5) to 16 (2^4). These residual switching states comprise 14 active and two null voltage vectors. Assuming that phase A is under fault, its current becomes zero, and its voltage is specified by the back electromotive force of the faulty phase. In this situation, the mathematical relation between the four healthy phase voltages and the available switching states can be established as

$$\begin{bmatrix} V_B \\ V_C \\ V_D \\ V_E \end{bmatrix} = \frac{U_{DC}}{4} \begin{bmatrix} 3 & -1 & -1 & -1 \\ -1 & 3 & -1 & -1 \\ -1 & -1 & 3 & -1 \\ -1 & -1 & -1 & 3 \end{bmatrix} \begin{bmatrix} S_B \\ S_C \\ S_D \\ S_E \end{bmatrix} \tag{1}$$

where V_k and S_k (k=B, C, D, E) are the phase voltages and switching states of each inverter leg, respectively. S_k can acquire two binary states: state 1 for upper switch ON and lower OFF and state 0 for the reverse case.

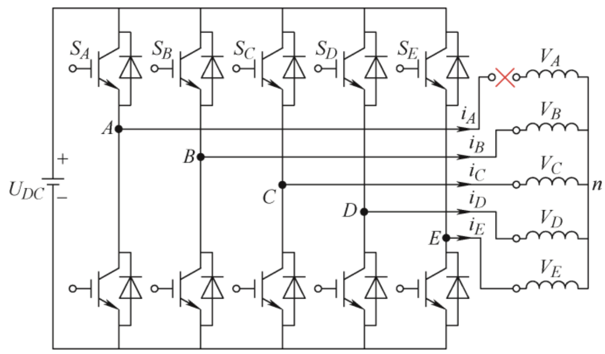

Fig. 1 Five-phase drive system under open-circuit fault

For post-fault operation, a normal five-phase decoupling transformation is inappropriate. Therefore, a reduced vector space decomposition (VSD) transformation [27], which considers the asymmetrical behavior of the faulty drive system, is employed to plot the five-phase variables on two stationary subspaces. Namely, the α-β subspace and the x-y subspace; the first subspace is composed of variables that contribute to the electromechanical energy conversion, and the second subspace variables do not produce torque. However, they cause undesirable harmonics and losses. As a result, these subspaces are referred to as the fundamental and harmonic subspaces, respectively. In addition, the zero-sequence component of the system is illustrated by the z-axis. In the post-fault condition, the control degree of freedom is reduced, and the control of the components in the direction of the x-axis is lost. Therefore, only the α-axis, β-axis, and y-axis components are controllable in a single-phase open-circuited faulty drive. The reduced decoupling transformation is given by Eq. (2) and the available post-fault voltage vectors in the two subspaces are shown in Fig. 2. In addition, the switching state of each active voltage vector is given in the second column of Tab. 1. The switching states of the two null vectors $\boldsymbol{V}_0$ and $\boldsymbol{V}_{15}$ are 0000 and 1111, respectively.

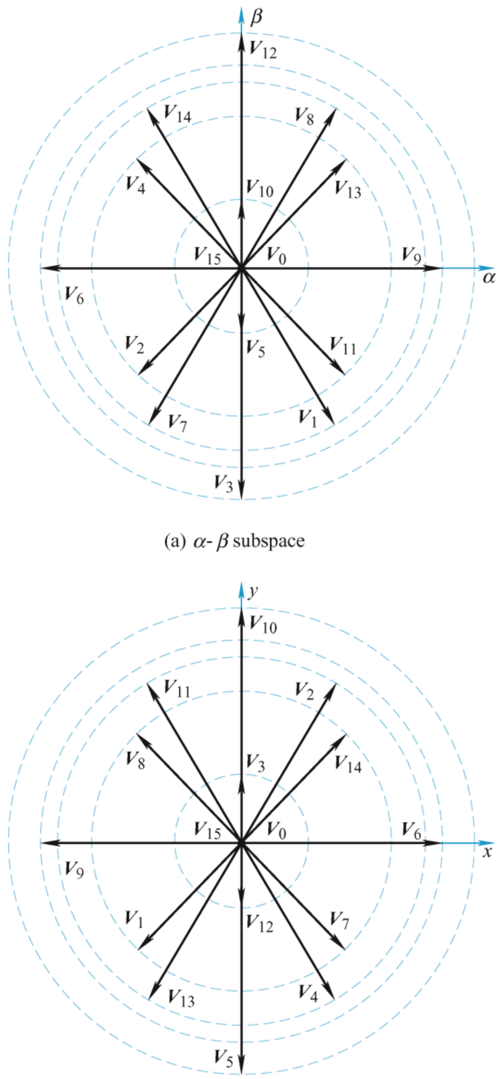

Fig. 2 Available voltage vectors under open-circuit fault

Tab. 1 Virtual voltage vectors synthesis principles

VV_i	V_u,V_v	C	$\|VV_i\|$
VV_1	V_9 (1001)	1	$0.447\,2U_{DC}$
VV_2	V_{13} (1101),V_8 (1000)	0.382	$0.394\,4U_{DC}$
VV_3	V_{12} (1100),V_8 (1000)	0.618	$0.532\,6U_{DC}$
VV_4	V_{12} (1100),V_{14} (1110)	0.618	$0.532\,6U_{DC}$
VV_5	V_4 (0100),V_{14} (1110)	0.382	$0.394\,4U_{DC}$
VV_6	V_6 (0110)	1	$0.447\,2U_{DC}$
VV_7	V_2 (0010),V_7 (0111)	0.382	$0.394\,4U_{DC}$
VV_8	V_3 (0011),V_7 (0111)	0.618	$0.532\,6U_{DC}$
VV_9	V_3 (0011),V_1 (0001)	0.618	$0.532\,6U_{DC}$
VV_{10}	V_{11} (1011),V_1 (0001)	0.382	$0.394\,4U_{DC}$

$$\boldsymbol{D}_{FT}=\frac{2}{5}\begin{bmatrix}\cos\delta-1 & \cos2\delta-1 & \cos3\delta-1 & \cos4\delta-1\\ \sin\delta & \sin2\delta & \sin3\delta & \sin4\delta\\ \sin2\delta & \sin4\delta & \sin6\delta & \sin8\delta\\ 1 & 1 & 1 & 1\end{bmatrix} \tag{2}$$

where δ=2π/5. It is clear from Fig. 2 that V_x=$-V_\alpha$. The park transformation is given by Eq. (3), which converts the α-β subspace components into a synchronous reference frame representation (d-q subspace). In this work, the rotational transformation for the x-y subspace components is useless, as the y-axis components in the x-y subspace will theoretically be eliminated in order to construct harmonic-less virtual vectors in the α-β subspace, as described in Section 3.1.

$$\boldsymbol{R}(\theta)=\begin{bmatrix}\cos\theta & \sin\theta & 0 & 0\\ -\sin\theta & \cos\theta & 0 & 0\\ 0 & 0 & 1 & 0\\ 0 & 0 & 0 & 1\end{bmatrix} \tag{3}$$

where θ indicates the rotor position. The reduced transformation matrix in Eq. (2) has made it possible to utilize the same motor predictive models in the pre-fault and post-fault operations. Therefore, the normal current predictive model can be employed for the post-fault condition, which is expressed as

$$\begin{cases} i_d^{k+1}=\left(1-\dfrac{R_sT_s}{L_d}\right)i_d^k+\omega_eT_si_q^k+\dfrac{V_d^kT_s}{L_d}\\ i_q^{k+1}=\left(1-\dfrac{R_sT_s}{L_q}\right)i_q^k-\omega_eT_si_d^k+\dfrac{V_q^kT_s}{L_q}-\dfrac{\omega_e\psi_{pm}}{L_q}\end{cases} \tag{4}$$

where i_d and i_q are the d-q axis currents, and V_d and V_q are the d-q axis voltages. R_s is the stator resistance, L_d and L_q are the d-q axis inductances, ω_e is the electrical speed, ψ_{pm} is the permanent magnet flux linkage, and T_s is the control period. The superscripts k and k+1 represent the real-time and one-step predicted values, respectively. To compensate for the delay produced by hardware limitations, predictions at time k+2 are derived as

$$\begin{cases} i_d^{k+2}=\left(1-\dfrac{R_sT_s}{L_d}\right)i_d^{k+1}+\omega_eT_si_q^{k+1}+\dfrac{V_d^{k+1}T_s}{L_d}\\ i_q^{k+2}=\left(1-\dfrac{R_sT_s}{L_q}\right)i_q^{k+1}-\omega_eT_si_d^{k+1}+\dfrac{V_q^{k+1}T_s}{L_q}-\dfrac{\omega_e\psi_{pm}}{L_q}\end{cases} \tag{5}$$

3 Proposed fault-tolerant DB-MPCC-SVPWM

The proposed fault-tolerant DB-MPCC-SVPWM control scheme can be divided into three subsections. Initially, harmonic-less virtual voltage vectors are created and their amplitudes are adjusted. Subsequently, the reference voltage vector is estimated in the new virtual vector space distribution by employing the deadbeat principle on the motor predictive model. Finally, a modified fault-tolerant SVPWM strategy is developed and implemented.

3.1 Post-fault virtual vector space distribution and amplitude adjustment

To achieve the minimum copper loss condition, the *x*-*y* subspace shown in Fig. 2b should be regulated. However, under fault conditions, only the *y*-axis current can be controlled. Therefore, the *y*-axis voltage vectors can be constrained to an average of zero by synthesizing the virtual voltage vectors from the fundamental vectors with specific ratios in the α-β subspace. In Ref. [14], a redesigned space vector distribution of 10 virtual voltage vectors is presented, which ensures the elimination of harmonics along the *y*-axis and the symmetrical PWM realization. These virtual vectors are shown in Fig. 3a, and their synthesis principle is described as

$$\boldsymbol{VV}_i\left(\boldsymbol{V}_u,\boldsymbol{V}_v\right)=C\cdot\boldsymbol{V}_u+\left(1-C\right)\cdot\boldsymbol{V}_v \tag{6}$$

where $\boldsymbol{VV}_i$ (i=1, 2, 3,$\cdots$,10) are the virtual voltage vectors synthesized from two fundamental vectors $\boldsymbol{V}_u$ and $\boldsymbol{V}_v$ in the α-β subspace of Fig. 2a. C represents the dwell time of the first fundamental active vector, $\boldsymbol{V}_u$. However, the virtual vectors $\boldsymbol{VV}_1$ and $\boldsymbol{VV}_6$ comprise only a single fundamental active vector. In Tab. 1, the synthesis principles for the 10 virtual voltage vectors and their resultant amplitudes are listed. For example, the virtual vector $\boldsymbol{VV}_2$ is synthesized from the fundamental vectors V_{13} and V_8, with $C = 0.382$.

From Fig. 3a, it can be observed that the actual virtual vector distribution is irregular in terms of both amplitude and position. This irregularity can be reduced by adjusting the amplitude of the vectors. From Tab. 1, the amplitudes of $\boldsymbol{VV}_2$, $\boldsymbol{VV}_5$, $\boldsymbol{VV}_7$, and $\boldsymbol{VV}_{10}$ are 0.394 4U_{DC}. However, the other vectors are large and can be adjusted. Therefore, the maximum active durations of $\boldsymbol{VV}_1$ and $\boldsymbol{VV}_6$ are restricted to 0.88, whereas those of $\boldsymbol{VV}_3$, $\boldsymbol{VV}_4$, $\boldsymbol{VV}_8$, and $\boldsymbol{VV}_9$ are limited to 0.74, with the help of a null vector. Thus, the amplitude of each vector can be fixed to 0.394 4 U_{DC}, and the adjusted virtual vectors are illustrated in Fig. 3b. Although this adjustment shrinks the modulation zone, however the steady-state performance can be improved. Moreover, Fig. 3c shows the uncontrollable virtual voltage vectors along the *x*-axis, as their *y*-axis components are eliminated. These virtual vectors correspond to the vectors shown in Fig. 3b.

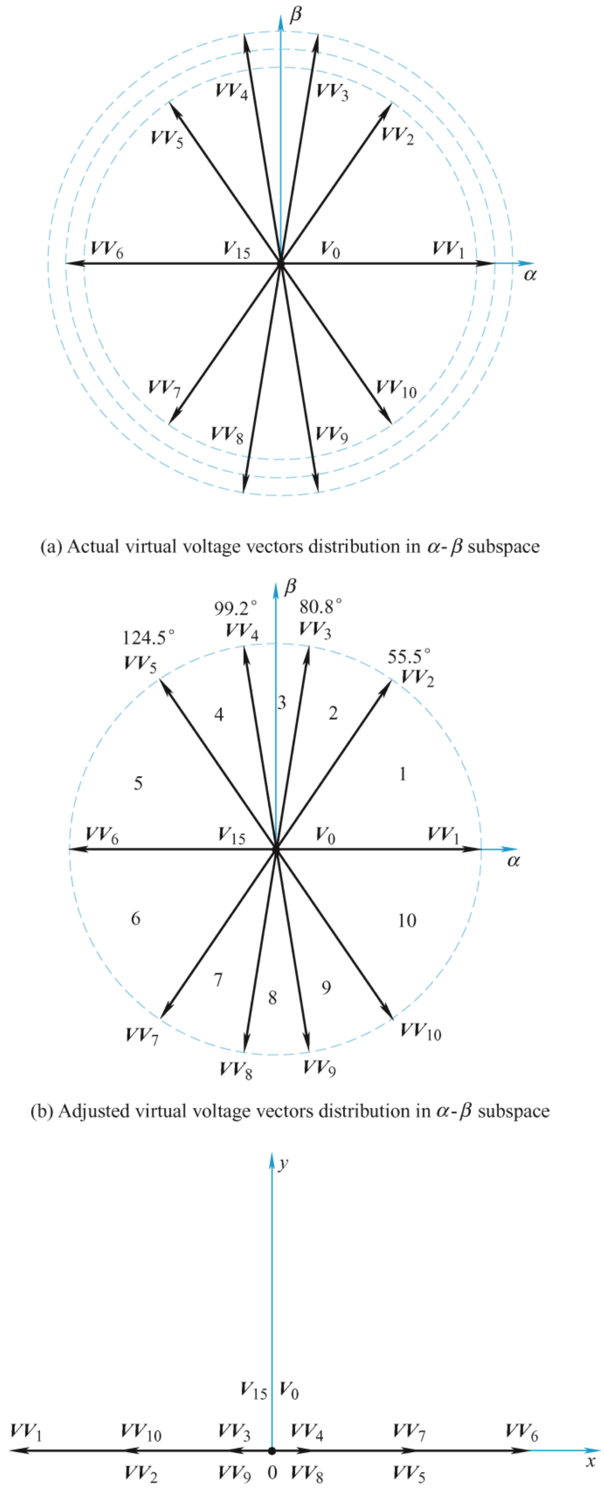

(a) Actual virtual voltage vectors distribution in α-β subspace

(b) Adjusted virtual voltage vectors distribution in α-β subspace

(c) Adjusted virtual voltage vectors along *x*-axis

Fig. 3 Post-fault virtual voltage vectors distribution

3.2 Reference voltage vector prediction

The deadbeat control principle is employed to predict the reference voltage vector. This method is simple, has a better dynamic response, and considers the nonlinearity of the system [18]. First, the delay-compensated current predictive model demonstrated in Eq. (5) is reorganized to construct the stator voltage predictive model. Second, the deadbeat current control principle is applied to the voltage predictive model. Finally, the reference voltages in the direction of the d-q axis are obtained. Therefore, this method is collectively referred to as the deadbeat model predictive current control (DB-MPCC).

The predictive model in Eq. (5) is rearranged to compute the d-q axis predicted voltages as

$$\begin{cases} V_d^{k+1} = L_d\left(\dfrac{i_d^{k+2}-i_d^{k+1}}{T_s}\right) + i_d^{k+1}R_s - \omega_e L_d i_q^{k+1} \\ V_q^{k+1} = L_q\left(\dfrac{i_q^{k+2}-i_q^{k+1}}{T_s}\right) + i_q^{k+1}R_s + \omega_e L_q i_d^{k+1} + \omega_e \psi_{pm} \end{cases} \tag{7}$$

According to the deadbeat current control principle, the current at the k+2 interval should reach the reference value at the k+1 interval. Therefore, the reference voltages can be estimated as

$$\begin{cases} V_d^* = L_d\left(\dfrac{i_d^*-i_d^{k+1}}{T_s}\right) + i_d^{k+1}R_s - \omega_e L_d i_q^{k+1} \\ V_q^* = L_q\left(\dfrac{i_q^*-i_q^{k+1}}{T_s}\right) + i_q^{k+1}R_s + \omega_e L_q i_d^{k+1} + \omega_e \psi_{pm} \end{cases} \tag{8}$$

The inverse park transformation is used to calculate the voltage references in a stationary frame.

3.3 Improved fault-tolerant SVPWM strategy

In this subsection, the conventional healthy five-phase SVPWM approach is extended to a new control set of 10 virtual voltage vectors with irregular space distribution in the post-fault condition, as shown in Fig. 3b. The modified strategy presents new expressions for the calculation of the switching durations or the application times of the voltage vectors being applied in a control period; meanwhile, the same traditional structure of SVPWM is well maintained.

In Fig. 3b, 10 natural sectors were defined. Each sector has two virtual vectors and two null vectors. In this case, the adjacent vectors $\boldsymbol{VV}_1$ and $\boldsymbol{VV}_2$ constitute sector 1, which ranges from 0° to 55.5°. The reference voltage vector is calculated using Eqs. (7) and (8). The position where the reference vector is located can be measured by a simple trigonometric rule and is denoted as γ.

It is assumed that the reference voltage vector ($\boldsymbol{V}_{REF}$) is located in sector 1, as shown in Fig. 4, in which γ indicates the position of the reference vector with respect to the α-axis. To synthesize $\boldsymbol{V}_{REF}$, virtual vectors $\boldsymbol{VV}_1$ and $\boldsymbol{VV}_2$, and null vectors $\boldsymbol{V}_0$ and $\boldsymbol{V}_{15}$ with the optimal switching durations are used. For example, T_a and T_b represent the durations of $\boldsymbol{VV}_1$ and $\boldsymbol{VV}_2$, respectively, and T_0 denotes the duration of the two null vectors. Moreover, T_s indicates one complete control period. According to the sine theorem, in sector 1

$$\frac{|\boldsymbol{VV}_1|T_a}{\sin(55.5^\circ-\theta)} = \frac{|\boldsymbol{V}_{REF}|T_s}{\sin(55.5^\circ)} = \frac{|\boldsymbol{VV}_2|T_b}{\sin\theta} \tag{9}$$

where $|\boldsymbol{V}_{REF}|$, $|\boldsymbol{VV}_1|$, and $|\boldsymbol{VV}_2|$ are the amplitudes of vectors $\boldsymbol{V}_{REF}$, $\boldsymbol{VV}_1$, and $\boldsymbol{VV}_2$, respectively. As shown in Fig. 3b, the adjusted amplitude of each virtual vector is 0.394 4U_{DC}. After solving Eq. (9), the expressions for T_a and T_b can be expressed as

$$\begin{cases} T_a = \dfrac{|\boldsymbol{V}_{REF}|\sin(55.5^\circ-\gamma)}{0.394\,4U_{DC}\sin(55.5^\circ)}T_s \\ T_b = \dfrac{|\boldsymbol{V}_{REF}|\sin\gamma}{0.394\,4U_{DC}\sin(55.5^\circ)}T_s \end{cases} \tag{10}$$

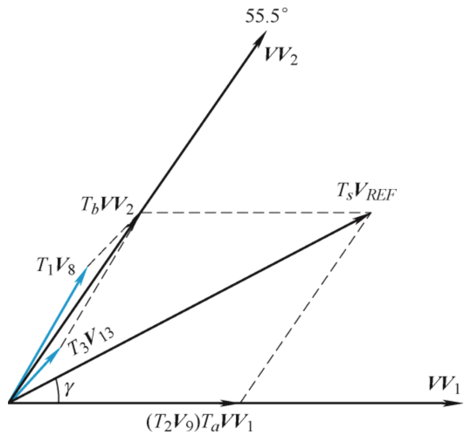

Fig. 4 Reference voltage vector synthesis in sector 1 with improved SVPWM

With the decomposition of $\boldsymbol{V}_{REF}$ into the α-axis and β-axis components, the following expressions in Eq. (11) can be introduced to generalize T_a and T_b

$$\begin{cases} V_\alpha^* = |V_{REF}|\cos\gamma \\ V_\beta^* = |V_{REF}|\sin\gamma \\ |V_{opt}| = 0.394\,4U_{DC} \\ a_1 = V_\alpha^*\sin(55.5^\circ) - V_\beta^*\cos(55.5^\circ) \\ a_2 = V_\alpha^*\sin(80.8^\circ) - V_\beta^*\cos(80.8^\circ) \\ a_3 = V_\alpha^*\sin(80.8^\circ) + V_\beta^*\cos(80.8^\circ) \\ a_4 = V_\alpha^*\sin(55.5^\circ) + V_\beta^*\cos(55.5^\circ) \end{cases} \tag{11}$$

where "*" is used to distinguish the reference variables and $|V_{opt}|$ represents the adjusted amplitude for all vectors. By comparing Eq. (10) with Eq. (11), T_a and T_b for sector 1 can be simplified as

$$\begin{cases} T_a = \dfrac{a_1 \cdot T_s}{|V_{opt}|\sin(55.5^\circ)} \\ T_b = \dfrac{V_\beta^* \cdot T_s}{|V_{opt}|\sin(55.5^\circ)} \end{cases} \tag{12}$$

However, for actual implementation, the switching durations of the fundamental vectors are required; these can be extracted from the durations of the virtual vectors. From Tab. 1 and Fig. 4, it can be observed that VV_1 is simply V_9, and VV_2 is originally synthesized from V_{13} and V_8 with dwell times of 0.382 and 0.618, respectively. Hence, T_a and T_b can be distributed into their respective durations of the fundamental active vectors. The switching durations for V_8, V_9, and V_{13} in sector 1 are denoted by T_1, T_2, and T_3, respectively, and can be expressed as

$$\begin{cases} T_1 = 0.618T_b \\ T_2 = T_a \\ T_3 = 0.382T_b \\ T_0 = T_s - T_1 - T_2 - T_3 \end{cases} \tag{13}$$

By following the same procedure for the other sectors, the switching durations of the virtual and corresponding fundamental voltage vectors can be evaluated, and their expressions are listed in Tab. 2. In this table, S represents the sector number, T_a and T_b are the durations of the virtual vectors, and, T_1, T_2 and T_3 are the durations of the fundamental vectors.

Tab. 2 Switching durations

S	T_a	T_b	T_1,T_2,T_3	S	T_a	T_b	T_1, T_2, T_3
1	$\frac{a_1T_s}{\lvert V_{opt}\rvert\sin(55.5^\circ)}$	$\frac{V_\beta^*T_s}{\lvert V_{opt}\rvert\sin(55.5^\circ)}$	$T_1=0.618T_b$ $T_2=T_a$ $T_3=0.382T_b$	6	$\frac{-a_1T_s}{\lvert V_{opt}\rvert\sin(55.5^\circ)}$	$\frac{-V_\beta^*T_s}{\lvert V_{opt}\rvert\sin(55.5^\circ)}$	$T_1=0.382T_b$ $T_2=T_a$ $T_3=0.618T_b$
2	$\frac{a_2T_s}{\lvert V_{opt}\rvert\sin(25.3^\circ)}$	$\frac{-a_1T_s}{\lvert V_{opt}\rvert\sin(25.3^\circ)}$	$T_1=0.618T_a+0.382T_b$ $T_2=0.618T_b$ $T_3=0.382T_a$	7	$\frac{-a_2T_s}{\lvert V_{opt}\rvert\sin(25.3^\circ)}$	$\frac{a_1T_s}{\lvert V_{opt}\rvert\sin(25.3^\circ)}$	$T_1=0.382T_a$ $T_2=0.618T_b$ $T_3=0.618T_a+0.382T_b$
3	$\frac{a_3T_s}{\lvert V_{opt}\rvert\sin(18.4^\circ)}$	$\frac{-a_2T_s}{\lvert V_{opt}\rvert\sin(18.4^\circ)}$	$T_1=0.382T_a$ $T_2=0.618T_a+0.618T_b$ $T_3=0.382T_b$	8	$\frac{-a_3T_s}{\lvert V_{opt}\rvert\sin(18.4^\circ)}$	$\frac{a_2T_s}{\lvert V_{opt}\rvert\sin(18.4^\circ)}$	$T_1=0.382T_b$ $T_2=0.618T_a+0.618T_b$ $T_3=0.382T_a$
4	$\frac{a_4T_s}{\lvert V_{opt}\rvert\sin(25.3^\circ)}$	$\frac{-a_3T_s}{\lvert V_{opt}\rvert\sin(25.3^\circ)}$	$T_1=0.382T_b$ $T_2=0.618T_a$ $T_3=0.382T_a+0.618T_b$	9	$\frac{-a_4T_s}{\lvert V_{opt}\rvert\sin(25.3^\circ)}$	$\frac{a_3T_s}{\lvert V_{opt}\rvert\sin(25.3^\circ)}$	$T_1=0.382T_a+0.618T_b$ $T_2=0.618T_a$ $T_3=0.382T_b$
5	$\frac{V_\beta^*T_s}{\lvert V_{opt}\rvert\sin(55.5^\circ)}$	$\frac{-a_4T_s}{\lvert V_{opt}\rvert\sin(55.5^\circ)}$	$T_1=0.382T_a$ $T_2=T_b$ $T_3=0.618T_a$	10	$\frac{-V_\beta^*T_s}{\lvert V_{opt}\rvert\sin(55.5^\circ)}$	$\frac{a_4T_s}{\lvert V_{opt}\rvert\sin(55.5^\circ)}$	$T_1=0.618T_a$ $T_2=T_b$ $T_3=0.382T_a$

It should be noted that the sequence of application of voltage vectors is selected according to the symmetrical PWM requirement. For example, the optimal switching pattern in sector 1 is V_0-V_8-V_9-V_{13}-V_{15}-V_{13}-V_9-V_8-V_0. In Fig. 5, the symmetrical PWM pulses for sector 1 are illustrated, where each pulse is high in the middle of the control period T_s and low at the ends. Using a similar technique, PWM pulses for other sectors can be plotted. Thus, owing to the implementation of SVPWM, the constant switching frequency operation can be performed.

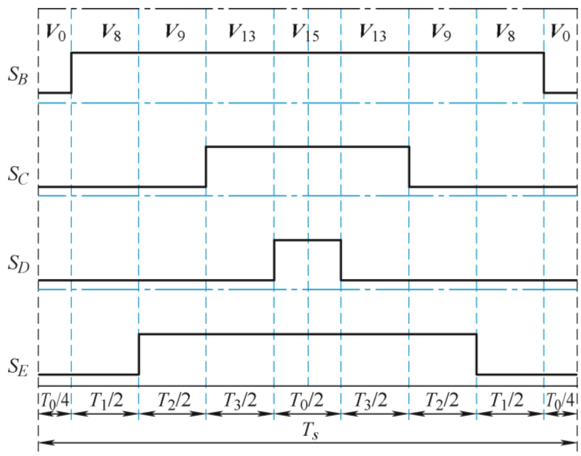

Fig. 5 Symmetrical PWM pulses for sector 1

Moreover, the duty cycles of the phase switches for sector 1 are expressed in Eq. (14)

$$\begin{cases} Duty_D = 0.5T_0/T_s \\ Duty_C = Duty_D + T_3/T_s \\ Duty_E = Duty_C + T_2/T_s \\ Duty_B = Duty_E + T_1/T_s \end{cases} \tag{14}$$

For the remaining sectors, the duty cycles can be determined using the same method.

Furthermore, in Fig. 6, the control diagram of the proposed fault-tolerant DB-MPCC-SVPWM strategy is presented. A speed PI controller outputs the q-axis current reference i^*_q, whereas the d-axis current reference i^*_d is fixed at zero. The predicted reference voltage vector is modulated using an improved SVPWM stage.

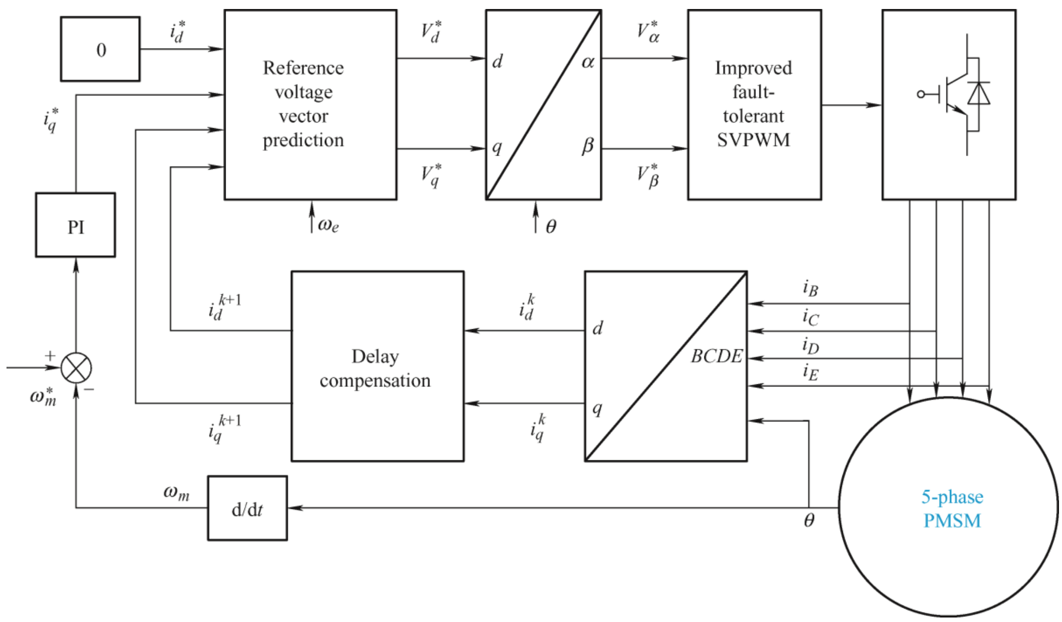

Fig. 6 Control diagram of proposed DB-MPCC-SVPWM

4 Experimental verification

The superiority of the proposed scheme was validated by experiments on a five-phase PMSM drive setup, as shown in Fig. 7. The motor parameters are presented in Tab. 3. The control algorithms were implemented in a TI TMS320F28377 digital signal processor. The torque load was provided by a DC motor connected to the resistor. The speed, torque, and stator phase current waveforms were displayed on an oscilloscope and measured with an incremental encoder, a torque sensor, and a current sensor, respectively. The rated torque of the five-phase PMSM is 10 N • m.

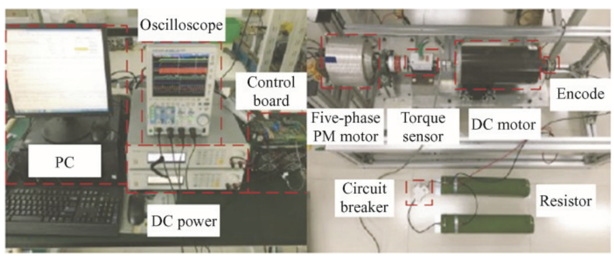

Fig. 7 Experimental setup of five-phase PMSM drive system

Tab. 3 Parameters of PMSM

Parameter	Value
Rated speed/(r/min)	450
Flux-linkage/Wb	0.029
L_d/mH, L_q/mH	3.1
R_s/Ω	1
Poles pairs n	31

For experimental verification, the proposed DB-MPCC-SVPWM scheme was compared with an existing fault-tolerant virtual voltage vector-based finite control set model predictive current control (FCS-MPCC-VV) strategy described in Ref. [13]. In this method, six virtual voltage vectors are used as candidate control set to evaluate the cost function, and a single selected optimal virtual vector is applied in one control period.

However, with the same sampling period T_s, the switching frequency of the existing scheme is lower than that of the proposed method. Therefore, for a fair comparison, a similar average switching frequency of approximately 20 kHz was considered for the two strategies. The sampling period of the proposed scheme is 50 μs, and that of the existing strategy is 40 μs. In the following sections, the steady-state and dynamic performance of the two schemes under identical operating conditions is analyzed.

4.1 Steady-state performance

A steady-state performance comparison was conducted between the two schemes, and their rotor speed, torque, and phase B current responses are presented in Fig. 8. The speed and load torque references were set to 200 r/min and 4 N • m, respectively. However, the tested maximum load capacity of the proposed fault-tolerant scheme was 8.5 N • m. The torque quality was examined by the ripple value calculated using Eq. (15). The Fourier transform analysis of the phase B current provides the total harmonic distortion (THD) percentage for each scheme, and Fig. 9 illustrates this analysis. Another important factor for comparison is the computational load of the control strategies, which indicates the level of online complexity. In Tab. 4, the torque ripple value, THD, 3rd harmonic percentage, and execution time are listed for inspection of both methods.

$$T_{e\_r} = \sqrt{\frac{1}{n}\sum_{i=1}^{n}\left(T_{e\_i} - T_{e\_avg}\right)^2} \tag{15}$$

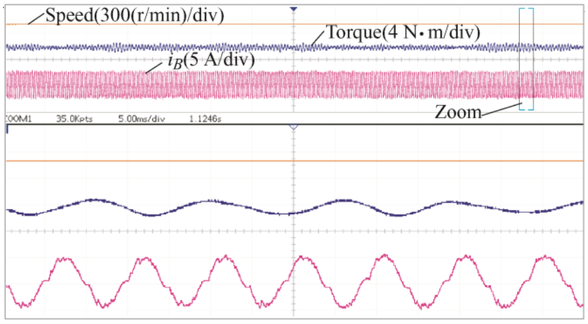

(a) Existing FCS-MPCC-VV

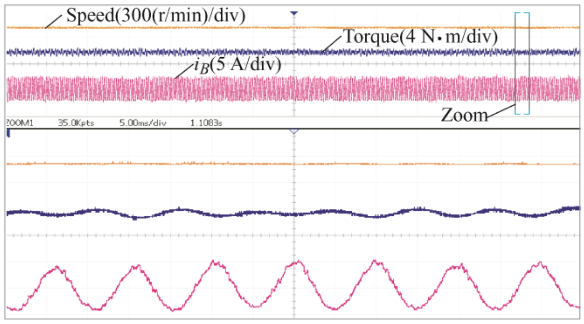

(b) Proposed DB-MPCC-SVPWM

Fig. 8 Steady-state performance of speed, torque and phase B current

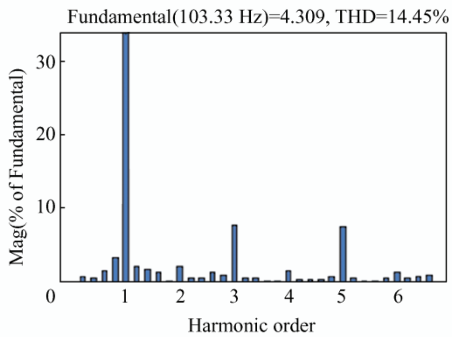

(a) Existing FCS-MPCC-VV

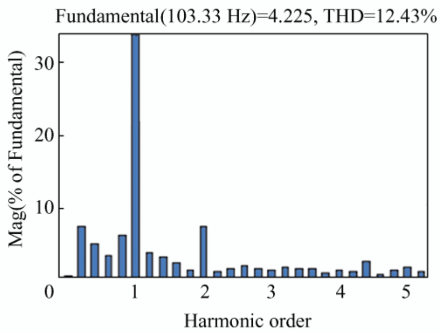

(b) Proposed DB-MPCC-SVPWM

Fig. 9 Fourier transform analysis of phase B current

Tab. 4 Steady-state performance comparison

	Existing FCS-MPCC-VV	Proposed DB-MPCC-SVPWM
T_{e_r}/(N • m)	0.71	0.36
THD_B(%)	14.45	12.43
3rd harmonic(%)	7.93	0.91
Execution-time/μs	30.2	21.6

Fig. 8 exhibits the torque responses; the proposed scheme shows a significant improvement in torque smoothness after a reduction in the torque ripple. The calculated torque ripple in the proposed scheme is 0.36 N •m, which is much lower than 0.71 N •m in the existing method. The reason for this enhancement of the torque quality in the proposed strategy is the synthesis of the reference voltage vector with space vector modulation. However, in the existing FCS-MPCC-VV method, the application of a single virtual voltage vector in one control period cannot always satisfy the optimal vector demand. Moreover, the phase B current of the proposed scheme is more sinusoidal than that of the existing strategy. From Fig. 9, the THD percentage of the proposed fault-tolerant scheme is 12.43%, and that of the existing method is 14.45%. The 3^{rd} and 5^{th} order harmonics in the phase B current of the proposed scheme are suppressed well. This suppression of the low-order harmonics is due to the adoption of SVPWM, which confirms the sinusoidal output voltage. However, the symmetrical SVPWM in the proposed scheme causes the 2^{nd} order harmonic to be the major harmonic component [22]. Furthermore, as shown in Fig. 10, the y-axis harmonic current is relatively well regulated in both strategies.

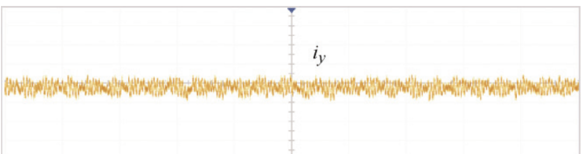

(a) Existing FCS-MPCC-VV

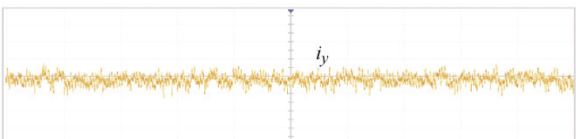

(b) Proposed DB-MPCC-SVPWM

Fig. 10 Steady-state performance of y-axis current

The computational load of the two schemes was assessed from the time taken to execute their code. At the start of code execution, a high level is generated from an I/O port, and this high level is changed to a low level at the end of the execution process. The duration of the high level, which represents the execution time, was measured. The calculated execution time of the proposed scheme was 21.6 μs and that of the existing method was 30.2 μs. This demonstrates that the computational load was reduced by 28% in the proposed strategy, a result that agrees with the theoretical prospects and proves its effectiveness. The reason for this reduction is the adoption of DB-MPCC, which deals with the optimization problem as a prediction of the reference voltage vector, and the cost function is not used. In addition, this reduction permits an increase in the sampling frequency, and thus, the control performance can be improved further. On the other hand, the exhaustive exploration process and cost function evaluations for the optimal vector selection in the existing FCS-MPCC-VV method cause a high computational load. Consequently, it can be concluded that the steady-state performance of the proposed scheme is superior, and its computational complexity is lower.

4.2 Dynamic performance

The dynamic performance of the two schemes was tested for their responses to variations in the reference speed and load torque. In the first test, the speed step response or the motor starting operation was analyzed. Fig. 11 illustrates the starting operation from standstill to 400 r/min. It can be observed that the actual speed in both methods rapidly responds to its reference, and it reaches the reference in less than 1 s without any noticeable overshot. The measured response time for the existing scheme is 0.68 s and that for the proposed one is 0.79 s. Meanwhile, the torque changes with speed as the resistor module is used in the load. In addition, the phase B current response was good in the two methods. Thus, the proposed scheme preserves the desired fast speed dynamic response of the existing FCS-MPCC-VV strategy.

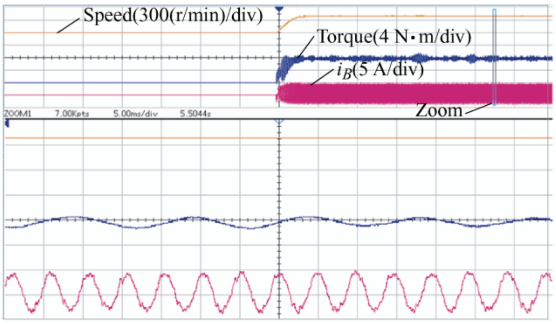

(a) Existing FCS-MPCC-VV

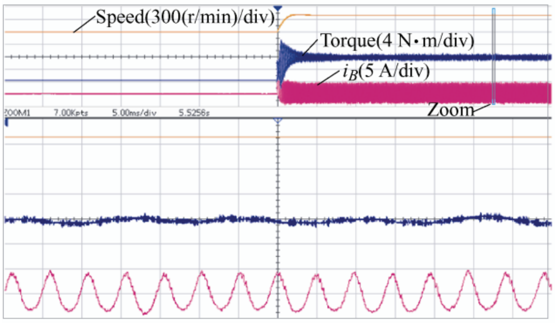

(b) Proposed DB-MPCC-SVPWM

Fig. 11 Dynamic performance of speed step: 0 r/min to 400 r/min

The second test results are presented in Fig. 12, where the external load disturbance response is examined. The reference speed was fixed at 400 r/min and the load torque was initially set to 4 N • m. At 4 s, the load torque suddenly increased to 8 N • m and returned to 4 N • m after approximately 5 s. It can be seen that the torque dynamic responses of the two schemes are rapid and almost identical, as the torque reference is attained within 1 s in both methods. At the points of load steps, the speed is disturbed, and stabilizes quickly in the proposed scheme. However, this difference was not very significant. Therefore, it can be concluded that the proposed fault-tolerant control approach offers adequate robustness to external load variations.

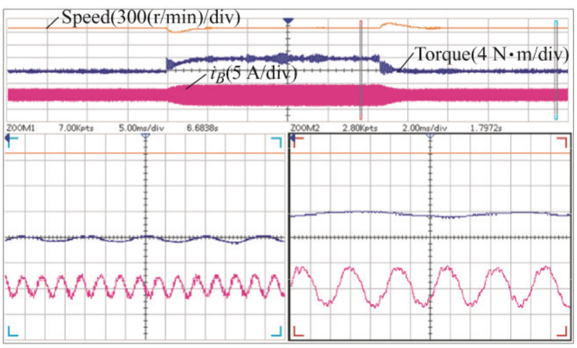

(a) Existing FCS-MPCC-VV

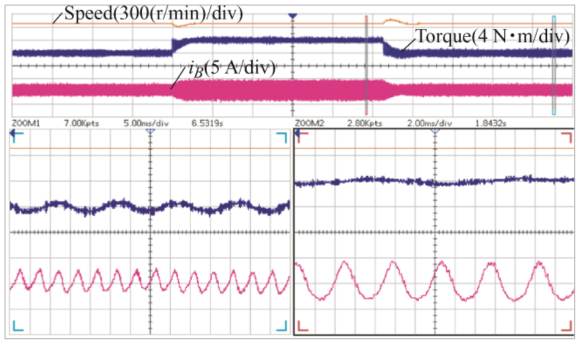

(b) Proposed DB-MPCC-SVPWM

Fig. 12 Dynamic performance of load variation: 4 N • m to 8 N • m to 4 N • m

5 Conclusions

This study has proposed and implemented a fault-tolerant DB-MPCC scheme with an improved SVPWM, which is based on a redesigned and adjusted space vector distribution under a single-phase open-circuit fault. In this strategy, the reference voltage vector is predicted using the deadbeat control principle. The newly developed SVPWM algorithm uses a predicted reference voltage vector to generate symmetrical PWM pulses. During the experiments, the proposed control presented effective merits in comparison with an existing FCS-MPCC-VV scheme. In the proposed approach, the computational load is significantly reduced with the use of the DB-MPCC method, where the cost function is avoided. Meanwhile, owing to the adoption of the SVPWM stage, the torque ripple and harmonic distortion in the phase currents are reduced significantly. In addition, the proposed fault-tolerant scheme demonstrates a fast dynamic robustness against speed and external load variations similar to that of the existing FCS-MPCC.

References

[1] B Wu, D Xu, J Ji, et al. Field-oriented control and direct torque control for a five-phase fault-tolerant flux-switching permanent-magnet motor. *Chin. J. Electr. Engin.*, 2018, 4(4): 48-56.

[2] M J Duran, F Barrero. Recent advances in the design, modeling, and control of multiphase machines-Part II. *IEEE Trans. Ind. Electron.*, 2016, 63(1): 459-468.

[3] W Zhang, Y Xu, Y Huang, et al. Reduction of high-frequency vibration noise for dual-branch three-phase permanent magnet synchronous motors. *Chin. J.*

Electr. Engin., 2020, 6(2): 42-51.

[4] A Salem, M Narimani. A review on multiphase drives for automotive traction applications. *IEEE Trans. Transport. Electrific*., 2019, 5(4): 1329-1348.

[5] K Nounou, J F Charpentier, K Marouani, et al. Emulation of an electric naval propulsion system based on a multiphase machine under healthy and faulty operating conditions. *IEEE Trans. Veh. Tech*., 2018, 67(8): 6895-6905.

[6] R Kianinezhad, B Nehid-Mobarakeh, L Baghli, et al. Modeling and control of six-phase symmetrical induction machine under fault condition due to open phases. *IEEE Trans. Ind. Electron*., 2008, 55(5): 1966-1977.

[7] A S Abdel-Khalik, S Ahmed, A A Elserougi, et al. Effect of stator winding connection of five-phase induction machines on torque ripples under open line condition. *IEEE/ASME Trans. Mechatronics*, 2015, 20(2): 580-593.

[8] Y Zhang, X Wang, H Yang, et al. Robust predictive current control of induction motors based on linear extended state observer. *Chin. J. Electr. Engin*., 2021, 7(1): 94-105.

[9] S Vazquez, J Rodriguez, M Rivera, et al. Model predictive control for power converters and drives: Advances and trends. *IEEE Trans. Ind. Electron*., 2017, 64(2): 935-947.

[10] W Huang, W Hua, F Chen, et al. Model predictive current control of open-circuit fault-tolerant five-phase flux-switching permanent magnet motor drives. *IEEE J. Emerg. Sel. Topics Power Electron*., 2018, 6(4): 1840-1849.

[11] H Lu, J Li, R Qu, et al. Fault-tolerant predictive control of six-phase PMSM drives based on pulse-width modulation. *IEEE Trans. Ind. Electron.*, 2019, 66(7): 4992-5003.

[12] W Huang, W Hua, F Chen, et al. Model predictive torque control with SVM for five-phase PMSM under open-circuit fault condition. *IEEE Trans. Power Electron*., 2020, 35(5): 5531-5540.

[13] T Tao, W Zhao, Y Du, et al. Simplified fault-tolerant model predictive control for a five-phase permanent-magnet motor with reduced computation burden. *IEEE Trans. Power Electron*., 2020, 35(4): 3850-3858.

[14] T Tao, W Zhao, Y He, et al. Enhanced fault-tolerant model predictive current control for a five-phase PM motor with continued modulation. *IEEE Trans. Power Electron*., 2021, 36(3): 3236-3246.

[15] A D Alexandrou, N K Adamopoulos, A G Kladas. Development of a constant switching frequency deadbeat predictive control technique for field oriented synchronous permanent-magnet motor drive. *IEEE Trans. Ind. Electron.*, 2016, 63(8): 5167-5175.

[16] X Yuan, S Zhang, C Zhang. Enhanced robust deadbeat predictive current control for PMSM drives. *IEEE Access*, 2019, 7: 148218-148230.

[17] Y Wang, X Wang, W Xie, et al. Deadbeat model-predictive torque control with discrete space-vector modulation for PMSM drives. *IEEE Trans. Ind. Electron*., 2017, 64(5): 3537-3547.

[18] M S R Saeed, W Song, B Yu, et al. Low-complexity deadbeat model predictive current control with duty ratio for five-phase PMSM drives. *IEEE Trans. Power Electron.*, 2020, 35(11): 12085-12099.

[19] W Zhao, H Wang, T Tao, et al. Model predictive torque control of five-phase PMSM by using double virtual voltage vectors based on geometric principle. *IEEE Trans. Transp Electrif.*, 2021, DOI: 10.1109/TTE.2021.3063193.

[20] F Bu, T Pu, Q Liu, et al. Four-degree-of-freedom overmodulation strategy for five-phase space vector pulse width modulation. *IEEE J. Emerg. Sel. Topics Power Electron*., 2021, 9(2): 1578-1590.

[21] J I Leon, S Kouro, L G Franquelo, et al. The essential role and the continuous evolution of modulation techniques for voltage-source inverters in the past, present, and future power electronics. *IEEE Trans. Ind. Electron.*, 2016, 63(5): 2688-2701.

[22] G Liu, L Qu, W Zhao, et al. Comparison of two SVPWM control strategies of five-phase fault-tolerant permanent-magnet motor. *IEEE Trans. Power Electron.*, 2016, 31(9): 6621-6630.

[23] Q Chen, L Gu, Z Lin, et al. Extension of space-vector-signal-injection-based MTPA control into SVPWM fault-tolerant operation for five-phase IPMSM. *IEEE Trans. Ind. Electron.*, 2020, 67(9): 7321-7333.

[24] J Zhang, L Li, D G Dorrell, et al. Modified PI controller with improved steady-state performance and comparison with PR controller on direct matrix converters. *Chin. J. Electr. Engin*., 2019, 5(1): 53-66.

[25] F Briz, M Hinkkanen. Design, implementation and performance of synchronous current regulators for AC drives. *Chin. J. Electr. Engin*., 2018, 4(3): 53-65.

[26] C S Lim, E Levi, M Jones, et al. FCS-MPC- based current control of a five-phase induction motor and its comparison with PI-PWM control. *IEEE Trans. Ind. Electron*, 2014, 61(1): 149-163.

[27] H Guzman, M J Duran, F Barrero, et al. Speed control of five-phase induction motors with integrated open-phase fault operation using model-based predictive current control techniques. *IEEE Trans. Ind. Electron.*, 2014, 61(9): 4474-4484.

Suleman Saeed received the B.Sc. degree in Electrical Engineering from COMSATS University Islamabad, Wah Cantt, Pakistan, in 2018. Currently, he is working toward the M.Sc. degree in Electrical Engineering from Jiangsu University, Zhenjiang, China. His research interests include control of multi-phase permanent-magnet machines and power electronics.

Wenxiang Zhao (M'08-SM'14) received the B.Sc. and M.Sc. degrees in Electrical Engineering from Jiangsu University, Zhenjiang, China, in 1999 and 2003, respectively, and the Ph.D. degree in Electrical Engineering from Southeast University, Nanjing, China, in 2010.

He has been with Jiangsu University since 2003, where he is currently a Professor with the School of Electrical Information Engineering. From 2008 to 2009, he was a Research Assistant with the Department of Electrical and Electronic Engineering, University of Hong Kong, Hong Kong, China. From 2013 to 2014, he was a Visiting Professor with the Department of Electronic and Electrical Engineering, University of Sheffield, Sheffield, UK. His current research interests include electric machine design, modeling, fault analysis, and intelligent control. He has authored and co-authored over 200 technical papers in these areas.

Huanan Wang received the B.Sc. degree in Electrical Engineering in Changzhou Institute of Technology, Changzhou, China, in 2018. He is currently working toward the M.Sc. degree in Electrical Engineering at Jiangsu University, Zhenjiang, China. His interest includes the control of multi-phase permanent-magnet machines.

Tao Tao received the B.Sc. degree in Electrical Engineering from Nanjing Agricultural University, Nanjing, China, in 2009, and the Ph.D. degrees from Jiangsu University, Zhenjiang, China, in 2020, all in Electrical Engineering.

He has been with Jiangsu University since 2021, where he is currently a Lecturer in the School of Electrical Information Engineering. His research interests include control of multi-phase permanent-magnet machines.

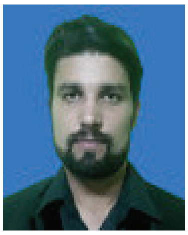

Faisal Khan was born in Utmanzai, Charsadda, Khyber Pakhtunkhwa, Pakistan, in 1986. He received the B.S. degree in Electronics Engineering and the M.S. degree in Electrical Engineering from the COMSATS Institute of Information Technology Islamabad, Abbottabad Campus, Pakistan, in 2009 and 2012, respectively, and the Ph.D. degree in Electrical Engineering from Universiti Tun Hussein Onn Malaysia, Malaysia, in 2017. From 2010 to 2012, he was a Lecturer with the University of Engineering and Technology, Peshawar, Abbottabad Campus. Since 2017, he has been an Assistant Professor with the Electrical and Computer Engineering Department, COMSATS University Islamabad, Abbottabad Campus, where he is currently the Head of Electric Machine Design Research Laboratory. He is the author of more than 100 publications. His research interests include design of flux-switching, synchronous, induction, linear, and dc machines. He received multiple research awards. He is a Member of IEEE and IEEE-IES Electrical Machines Technical Committee.